Applied Surface Science 536 (2021) 147841

Contents lists available at ScienceDirect

Applied Surface Science

journal homepage: www.elsevier.com/locate/apsusc

Synthesis and characterization of GaN/ReS_2, ZnS/ReS_2 and ZnO/ReS_2 core/shell nanowire heterostructures

Edgars Butanovs[a,*], Alexei Kuzmin[a], Sergei Piskunov[a], Krisjanis Smits[a], Aleksandr Kalinko[b], Boris Polyakov[a]

[a] Institute of Solid State Physics, University of Latvia, Kengaraga Street 8, Riga LV-1063, Latvia
[b] Department Chemie, Naturwissenschaftliche Fakultät, Universität Paderborn, Warburger Strasse 100, 33098 Paderborn, Germany

ARTICLE INFO

Keywords:
ReS_2
Layered materials
Core-shell nanowire
Electron microscopy
X-ray diffraction
Raman spectroscopy
X-ray absorption spectroscopy

ABSTRACT

Layered 2D van der Waals (vdW) materials such as graphene and transition metal dichalcogenides have recently gained a great deal of scientific attention due to their unique properties and prospective applications in various fields such as electronics and optoelectronics, sensors and energy. As a direct bandgap semiconductor in both bulk and monolayer forms, ReS_2 stands out for its unique distorted octahedral structure that results in distinctive anisotropic physical properties; however, only a few scalable synthesis methods for few-layer ReS_2 have been proposed thus far. Here, the growth of high-quality few-layer ReS_2 is demonstrated via sulfurization of a pre-deposited rhenium oxide coating on different semiconductor material nanowires (GaN, ZnS, ZnO). As-produced *core-shell* heterostructures were characterized by X-ray diffraction, scanning and transmission electron microscopy, micro-Raman spectroscopy and X-ray absorption spectroscopy. Experimental characterizations were supported by total energy calculations of the electronic structure of ReS_2 nanosheets and GaN, ZnS, and ZnO substrates. Our results demonstrate the potential of using nanowires as a template for the growth of layered vdW materials to create novel *core-shell* heterostructures for energy applications involving photocatalytic and electrocatalytic hydrogen evolution.

1. Introduction

Layered 2D van der Waals (vdW) materials such as graphene and transition metal dichalcogenides (TMDs) have recently gained a great deal of attention due to their unique properties when the bulk material is reduced to a monolayer [1–3], the wide variety of available materials [4] and their prospective applications in various fields, such as electronics and optoelectronics [5,6], sensors [7] and energy [8]. Currently, one of the main limitations on the use of these materials in practical devices is the growth of uniform, high-quality large-area films with controllable thicknesses [4,5]. Since the layers are bound together by weak vdW interactions, 2D materials to some extent do not need to satisfy the conventional semiconductor lattice matching requirement to grow well-crystallized epitaxial layers of different materials on top of each other [9,10]. Hence, the growth of high-quality 2D heterostructures of some of the most popular layered materials on various substrates has already been demonstrated [11,12], while techniques for growing more recently explored layered materials such as HfS_2 and ReS_2 are still being established [5,13].

The energy-related applications of TMD materials have recently attracted significant interest. For example, TMD materials can be used in supercapacitors, hydrogen evolution reactions and Li-ion battery (LIB) applications [14,15]. However, the bulk TMDs used in LIBs demonstrate rapid capacity fading. The engineering of novel 3D TMD-based hybrids is a potential approach to solving this issue and to improving the electrochemical performance of TMD nanomaterials [16]. One promising option is use of *core-shell* nanowire (NW) array architecture, in which the "core" is used as a high-mobility charge carrier channel, while the TMD-based "shell" is used for ion accumulation or electrochemical ion intercalation. This type of heterostructure design could also be used for efficient photocatalytic and electrocatalytic hydrogen evolution reactions. Very recently, the synthesis of novel TiO_2-ReS_2 *core-shell* heterostructures was reported by Wang *et al.* [17], and these have demonstrated very stable performance as a sodium-ion storage materials.

NWs are one-dimensional (1D) nanomaterials that exhibit promising properties e.g. for integration in electronic, optoelectronic and photonic functional devices [18,19]; moreover, their characteristics can be further improved by modification of their surfaces [20]. It has been shown that the surface of a NW has significantly smaller restriction on

* Corresponding author.
E-mail address: edgars.butanovs@cfi.lu.lv (E. Butanovs).

https://doi.org/10.1016/j.apsusc.2020.147841
Received 21 April 2020; Received in revised form 12 August 2020; Accepted 5 September 2020
Available online 11 September 2020
0169-4332/ © 2020 Elsevier B.V. All rights reserved.

the lattice mismatch of the materials and the stresses caused at the interface, in contrast to the conventional thin films growth [18,20,21], thus offering new possibilities of engineering novel hybrid *core-shell* nanostructures. The growth of various common 2D materials such as MoS_2 and WS_2 on different semiconductor NWs has been previously demonstrated [22–24], thus proving the possibility of using NWs as a prospective template for the growth of high-quality layered vdW materials, and even of achieving improved physical properties [23,25].

Similarly to other TMDs, ReS_2 consists of covalently bonded S-Re-S atomic planes, and these adjacent layers are coupled by weak vdW forces to form a bulk crystal [13]. It is important to note that unlike other 2D materials with an indirect-to-direct bandgap transition in monolayers, ReS_2 exhibits much weaker interlayer coupling, and therefore remains a direct bandgap ($E_g \sim 1.5$–1.6 eV) semiconductor in the bulk, few-layer and monolayer forms [26]. It possesses a unique distorted octahedral (1 T) structure [13] that results in anisotropic physical properties along the in-plane directions [27,28]. This anisotropy leads to distinctive optical properties [29], anisotropic electrical transport [28,30], thermal conductivity [31] and piezoresistive effect [32], which may be useful for emerging applications in electronics and optoelectronics [27] such as polarized light detection [33]. Other demonstrated applications of 2D ReS_2 include field-effect transistors [26,34,35], photodetectors [36–38], digital inverters [39], tunnel diodes [40], and photocatalytic and electrocatalytic hydrogen evolution (water splitting) [41].

Large-scale growth of uniform crystalline ReS_2 layers with controllable thickness is paramount for any practical applications. Mechanical exfoliation of a bulk crystal is commonly used in fundamental research [28,29,34,39] to obtain the highest quality crystals; however, this produces small mono- or few-layer flakes with uncontrollable position on the substrate, thereby making fabrication of devices more complicated. Chemical vapour transport (CVT) has been recently reported as a viable method of growing uniform ReS_2 films. He *et al.* [42] used metallic Re as a precursor to obtain high-quality ReS_2 flakes; however, due to the high melting point of Re (3180 °C), which gives rise to a low vapour pressure in the CVT system, this approach inevitably provides a low yield and a small growth rate of ReS_2. Several groups have demonstrated the growth of large-area ReS_2 at relatively low temperatures using ammonium perrhenate (NH_4ReO_4) [43], ReO_3 [36,44] or Re_2O_7 [45] as the rhenium precursor. The use of NH_4ReO_4 typically leads to poor crystal quality, mainly due to the high oxidation state of Re (+7) and unwanted byproducts [13]. Furthermore, Cui *et al.* [46] demonstrated that the synthesis temperature of ReS_2 can be lowered to 430 °C by forming a Re-Te eutectoid, thus producing large-area, high-crystallinity and uniform monolayers on mica with the tellurium-assisted CVT method. Since ReS_2 exhibits strong interlayer decoupling, out-of-plane growth is predominant on many substrates, including the widely used SiO_2/Si, leading to the growth of wrinkled low-quality polycrystalline films or thick flower-like ReS_2 via a typical CVT process [45]. Thus, ReS_2 is commonly grown on mica substrates due to its low surface energy [45,46], and on other 2D vdW materials such as graphene [44]. However, a crucial disadvantage of using mica is the need for a highly corrosive hydrofluoric acid for etching in order to delaminate the ReS_2 film from the substrate for further application [13]. Alternatively, sulfurization of a pre-deposited transition metal or transition metal oxide film has been successfully utilized for numerous TMDs to obtain high-quality mono- and few-layer films [47–50]. Urakami *et al.* [51] demonstrated the formation of ReS_2 films via the sulfurization of e-beam-deposited Re films on sapphire substrates, although a high temperature of 1100 °C was necessary. To the best of our knowledge, no previous reports on the sulfurization of pre-deposited rhenium oxide films to obtain few-layer ReS_2 have been published.

In this study, we demonstrated the growth of few-layer ReS_2 on different semiconductor material NWs (GaN, ZnS, ZnO) via the sulfurization of a pre-deposited rhenium oxide coating, and investigated the degree of ReS_2 crystallinity at different sulfurization temperatures. This two-step process allowed us to obtain high crystalline quality ReS_2 on different underlying materials in a medium temperature range. The results demonstrate the potential of using NWs as a template for growing layered vdW materials to produce novel hybrid *core-shell* nanostructures and 3D architectures. Furthermore, according to predictions made from our first principles calculations, these *core-shell* heterostructures could be used in efficient hydrogen evolution reactions [14].

2. Experimental section

2.1. Nanowire synthesis

GaN, ZnS and ZnO NWs were synthesised using an adapted atmospheric pressure chemical vapour transport method in a horizontal quartz tube reactor [24,52,53]. In all cases, the NWs were grown on oxidized silicon wafers SiO_2/Si(1 0 0) (*Semiconductor Wafer, Inc.*) coated with spherical Au nanoparticles (*Smart materials*, water suspension, 100 nm diameter) which were used as a catalyst for the vapour-liquid-solid (VLS) mechanism.

GaN NWs: 3 g metallic Ga (*99.999%, Alfa Aesar*) was loaded into a ceramic boat and placed in the centre of the quartz tube, and Au/Si substrates were placed downstream in a lower-temperature region. The reactor was heated to 920 °C under a flow of carrier gas mixture Ar/H_2-35%, and gaseous NH_3 flow in a 1:1 ratio to the carrier gas was then introduced and maintained for 30 min to enable the gas-phase reaction and NW growth, followed by natural cooling to room temperature under Ar/H_2 flow. As a result, GaN NWs of length 5–10 μm were produced on the SiO_2/Si substrate (see Fig. S1(a,b))

ZnS NWs: 0.4 g ZnS powder (> *97%, Sigma Aldrich*) was thermally evaporated in a quartz tube at a temperature of 950 °C for 30 min, followed by natural cooling. The vapour was carried downstream to the Au/Si substrate by N_2 gas to grow ZnS NWs of length 20–100 μm (see Fig. S1(c,d)).

ZnO NWs: A 1:1 mixture of ZnO and carbon powders was loaded into a ceramic boat in the centre of the quartz tube at 900 °C, and the vapour was transported downstream to the Au/Si substrate in a lower-temperature region using N_2 as a carrier gas. The temperature during growth was held constant for 90 min, followed by natural cooling to room temperature. As a result, ZnO NWs of length 10–50 μm were obtained on the SiO_2/Si substrate (see Fig. S1(e,f)).

2.2. ReS_2 synthesis

A simple two-step process was used to produce the ReS_2 shell surrounding the pure NW core: (1) a rhenium oxide (ReO_x) coating was sputter-deposited on top of the NW substrate followed by (2) sulfurization at elevated temperatures. First, an amorphous nonstoichiometric ReO_x coating was deposited via reactive DC magnetron sputtering of a metallic rhenium (Re) target in a mixed Ar/O_2 atmosphere (1 min at 100 W DC power) using a *Sidrabe SAF25/50* multifunctional cluster tool. Then, in order to convert rhenium oxide to ReS_2, as-prepared ReO_x samples were annealed for 20 min in a quartz tube reactor in a sulfur-rich atmosphere, which was created by placing sulfur powder upstream of the sample at 250 °C and using N_2 as a carrier gas. Different temperatures in the range 450–800 °C were used to study the degree of crystallinity of as-grown ReS_2. ReS_2 thin films on SiO_2/Si (1 0 0), and GaN-ReS_2, ZnS-ReS_2, ZnO-ReS_2 *core-shell* NWs were prepared.

As a reference sample, ReS_2 microcrystals were grown using the vapour transport method. In brief, a quartz ampoule was loaded with elemental precursor powders (Re and S) in stoichiometric proportions and a small amount of transport agent (iodine) powder was added. The quartz ampoule was then evacuated and sealed. A small temperature gradient was maintained between the ends of the ampoule ($T_{high} \sim 1100$ °C and $T_{low} \sim 1050$ °C) for several days, and the growth

of micrometre-sized ReS_2 monocrystals occurred at the low-temperature end.

2.3. Core-shell nanowire characterization

The morphology of the as-prepared *core-shell* NWs was characterized by scanning electron microscopy (SEM, Lyra, Tescan), whereas the inner crystalline structure was revealed by transmission electron microscopy (TEM, Tecnai GF20, FEI) operating at an accelerating voltage of 200 kV. Energy-dispersive X-ray spectroscopy (EDX) was used in both SEM and TEM to study the distribution of elements in the NWs. A selected-area electron diffraction (SAED) analysis was performed using CrysTBox software [54].

The phase composition of the samples was studied with X-ray diffraction (XRD) using a Rigaku MiniFlex 600 X-ray powder diffractometer with Bragg-Brentano θ-2θ geometry and a 600 W Cu anode (Cu Kα radiation, λ = 1.5406 Å) X-ray tube.

Micro-Raman spectroscopy measurements were performed using a TriVista 777 confocal Raman system (Princeton Instruments, 750 mm focal length, 1800 lines/mm grating) equipped with an upright Olympus microscope with Olympus UIS2 MPlanN 100x/0.90 objective, a continuous-wave single-frequency diode-pumped laser Cobolt Samba 150 (λ = 532 nm) and an Andor iDus DV420A-OE CCD camera.

X-ray absorption spectroscopy (XAS) measurements were performed at the HASYLAB/DESY PETRA-III P64 beamline [55]. The X-ray beam from the undulator was monochromatized with a Si(3 1 1) double-crystal monochromator, and the X-ray absorption near edge (XANES) spectra were recorded at the Re L_3-edge and Ga K-edge in fluorescence mode with a Passivated Implanted Planar Silicon (PIPS) detector (Canberra). All XAS measurements were made at room temperature.

2.4. Computational details

We carried out total energy first principles calculations on [0 0 0 1]-oriented mono- (ML), bi- (2ML), and three-layered (3ML) ReS_2 nanosheets, as well as 24-layer thick [1 –1 0 0] oriented slabs, in order to mimic the surfaces of GaN, ZnO and ZnS NWs. This was achieved by means of a HSE06 hybrid exchange-correlational functional [56] within density functional theory (DFT), as implemented in the computer code CRYSTAL17 [57]. Localized Gaussian-type functions (GTFs) in the form of atom-centred basis sets (BSs) were used for the expansion of periodic crystalline orbitals for Zn, S, and O, in the same way as in our recent study [20]. For Ga and N, full electron Triple-Zeta Valence BSs with polarization functions were adopted from [57], while effective-core pseudopotential BSs were used for Re [57]. The reliability of the chosen theoretical method was proven by calculations of band gap energy (δ) for the bulk phase of GaN, ZnS, ZnO, and ReS_2 crystals. Calculated band gaps for all of the materials under study showed good agreement with the experimentally observed results (see Fig. S6). To provide a balanced summation for both the direct and reciprocal lattices, reciprocal space integration was performed by sampling the Brillouin zone (BZ) with a 6 × 6 × 1 Pack-Monkhorst mesh [58], which resulted in a total of 20 k-points evenly distributed over the BZs. In each calculation of the fixed crystalline geometry, convergence was reached only when the total energy differed by less than 10^{-7} a. u. in two successive cycles of the self-consistent field (SCF) procedure [57]. Full geometry optimization was performed for all of the nanostructures considered in this study.

3. Results and discussion

NWs can be used as a template for the growth of layered vdW materials in order to conveniently study their inner crystalline structure via TEM. Fig. 1 shows TEM images of as-grown GaN-ReS_2 (a,b), ZnS-ReS_2 (c,d) and ZnO-ReS_2 (e,f) *core-shell* NWs prepared at 800 °C. The lower-magnification images show that GaN and ZnS NWs maintain their straight shape; however, ZnO NWs undergo a transition to an irregular shape, indicating the occurrence of a recrystallization process. The higher-magnification TEM images reveal the layered structure of the ReS_2 shell (which can be seen as parallel black and white lines along the NW surface) with a measured interlayer distance of around 6.3–6.4 Å for all samples, which closely matches the lattice constant a = 6.45 Å of triclinic ReS_2 [59]. The typical thickness of the ReS_2 shell varied from 2 to 10 monolayers (each consisting of S-Re-S atomic planes), and the shell was uniformly distributed over the length of the NWs with only slight variations in thickness. Furthermore, the single-crystalline nature of the core NWs is visible (in NWs with diameter less than 80 nm) indicating the high crystalline quality of the as-prepared *core-shell* heterostructures, as confirmed by SAED measurements. A detailed description of the SAED analysis is given in Fig. S2. Dominating (most intensive) diffraction spots typically belong to the NW core material, and are less intensive for the ReS_2 shell. The phases and crystallographic orientation were identified through a separate analysis of each pattern. The symmetric orientation of ReS_2 reflexes correlated with ZnO reflexes might indicate the epitaxial growth of ReS_2, while the SAED patterns of ReS_2 on ZnS and GaN do not exhibit epitaxial growth.

SEM images of the as-grown nanostructures (see Fig. 2) show that the length of the NWs was preserved, matching their respective pure NWs before the high-temperature treatment, and the density of the NW arrays was maintained. Similarly to TEM measurements, the morphology change of ZnO-ReS_2 NWs upon heating at 800 °C can also be observed by SEM.

To study the distribution of elements in the NWs, EDX measurements were performed (see Fig. 3). First, EDX elemental mapping along the length of the NWs was carried out via SEM to demonstrate the uniform distribution of ReS_2 axially over the underlying NWs. Next, cross-sectional EDX line scans were performed radially across the NWs using TEM, in order to prove the *core-shell* distribution of the elements. The elemental line scans show a localized core and shell with distinct interfaces in all studied NWs, a result that is consistent with the TEM images. It should be noted that the EDX intensity is usually not symmetric on both sides of the NW due to the sideways placement of the EDX detector in the electron microscope chamber.

Based on the TEM measurements, the optimal sulfurization temperature for obtaining high-quality monocrystalline ReS_2 layers from the magnetron-sputtered rhenium oxide coating was found to be 750–800 °C. Fig. S3 shows as ReS_2 shell converted at 750 °C that still exhibits a polycrystalline nature, as indicated by the non-parallel placement of the layers, while the TEM images in Fig. 1 shows a high degree of crystallinity at 800 °C. In the case of ZnO NWs, a structural change in the NW could be observed around 750 °C, and a further experiment was therefore performed. Fig. S4 shows TEM images of ZnO-ReS_2 NWs converted at 700 °C and 750 °C. It can clearly be seen that the ReS_2 is still polycrystalline at 700 °C, and becomes monocrystalline at higher temperatures, while the ZnO core re-crystallizes at 750 °C. It can be deduced that ZnO NWs undergo a sulfurization process at this temperature and are converted to the ZnS phase [22,60]. It is also worth noting that in our previous work [24], no detectable formation of the ZnS phase at 800 °C was observed in ZnO-WS_2 *core-shell* NWs due to the unique growth mechanism of the WS_2 shell.

To confirm the presence of phases in the as-grown *core-shell* NW samples, XRD measurements were performed on the NW arrays (converted at 800 °C) on Si(1 0 0)/SiO_2 substrates (see Fig. 4). All XRD patterns contained a strong ReS_2 (0 0 2) peak of the triclinic P-1 (No. 2) phase (ICDD-PDF #52-0818) as well as Bragg peaks, which were attributed to the Si(1 0 0) substrate (forbidden Si(2 0 0) reflection at 2θ ≈ 33°) and the gold nanoparticles used for VLS growth (ICDD-PDF #04-0784). For the GaN-ReS_2 and ZnS-ReS_2 NW samples, GaN (ICDD-PDF #50-0792) and ZnS (ICDD-PDF #36-1450) Bragg peaks are clearly apparent. For the ZnO-ReS_2 NWs samples, both ZnO (ICDD-PDF #36-1451) and ZnS phases were present, confirming that ZnO NWs are partly or fully converted to ZnS above 750 °C, as observed in the TEM measurements. It should be noted that the ratio between the ReS_2 and

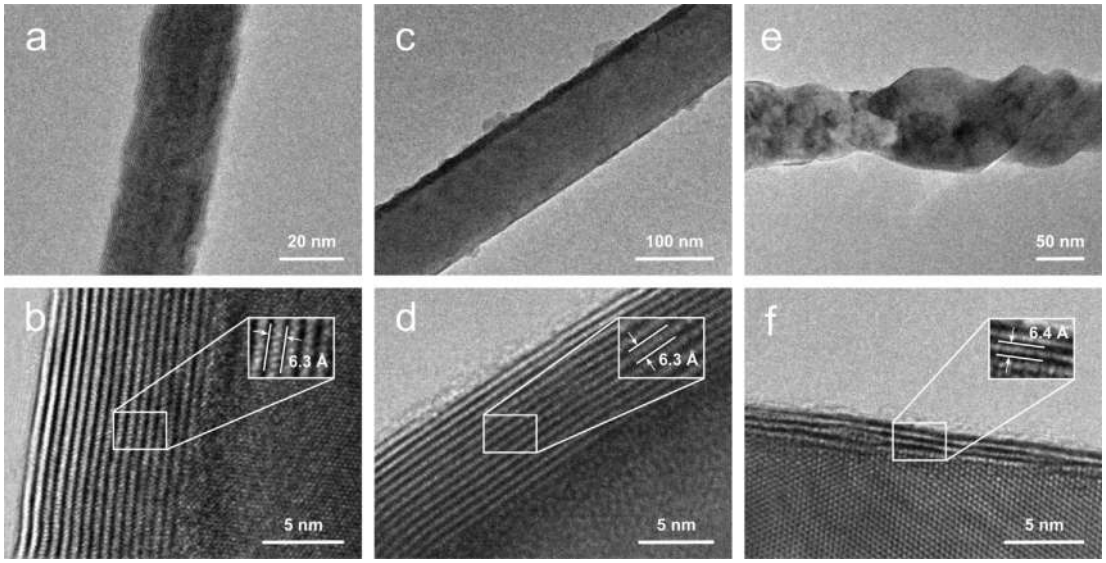

Fig. 1. Transmission electron microscope images at different magnifications for as-grown (a,b) GaN-ReS_2, (c,d) ZnS-ReS_2, and (e,f) ZnO-ReS_2 *core-shell* nanowires, prepared at 800 ˚C. The insets show the measured atomic interlayer distances between ReS_2 layers.

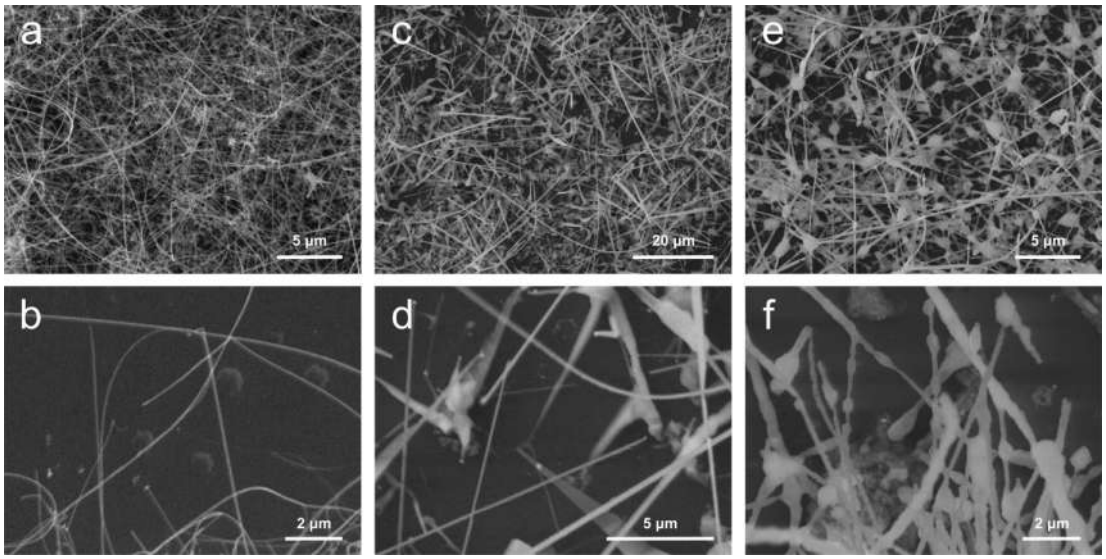

Fig. 2. Scanning electron microscope images of (a,b) GaN-ReS_2, (c,d) ZnS-ReS_2 and (e,f) ZnO-ReS_2 *core-shell* nanowires at different magnifications.

NW XRD peak intensities is related not only to the amount of ReS_2 on the NWs, but also to that on the Si(1 0 0)/SiO_2 substrate, hence, it cannot be used to quantitatively describe the phase composition ratio of the *core-shell* heterostructures. Since the ZnO NWs undergo the sulfurization process before the monocrystalline ReS_2 shell is formed, this material may not be a suitable template for ReS_2 growth, although it was possible to grow high-quality monocrystalline layers of ReS_2 on GaN and ZnS NWs.

Additional XRD measurements were performed on as-prepared ReS_2 thin film samples in order to investigate the degree of crystallinity over a wider range of sulfurization temperatures. Fig. S5 shows XRD patterns for ReS_2 thin films, converted at 450 ˚C, 700 ˚C and 1000 ˚C. The evolution of the ReS_2 (0 0 2) peak at 14.6˚ with increasing temperature can be clearly seen from the patterns, as the (0 0 4) and (0 0 6) peaks can be distinguished at very high temperatures [59]. This, therefore, confirms that the conversion of a rhenium oxide film in sulfur vapour is a viable method for obtaining crystalline ReS_2 thin films. The Bragg peak at 33˚ is attributed to diffraction at the SiO_2/Si(1 0 0) substrate, and no other phases were observed. XRD measurements indicated that a small amount of crystalline ReS_2 phase starts to appear even at 450 ˚C; however, the conversion rate becomes significant only at around 700 ˚C.

Micro-Raman scattering spectra for as-grown ZnO-ReS_2, ZnS-ReS_2 and GaN-ReS_2 *core-shell* NWs (measured in each case from a single NW) were compared with those of bulk ReS_2 microcrystals in Fig. 5. There are 12 atoms in the unit cell of triclinic (P-1) ReS_2 that give rise to 36 Γ-point phonon modes, of which 18 symmetric A_g modes are Raman active and nondegenerate [61]: these are indicated by vertical lines in Fig. 5. All of the Raman active phonon modes were observed in bulk ReS_2 and *core-shell* NWs. The Raman bands are narrower for bulk ReS_2 and GaN-ReS_2 NWs, and are slightly broadened for ZnO-ReS_2 and ZnS-ReS_2 NWs. This broadening leads to an overlap of the nearest bands located around 280 cm^{-1}, 307 cm^{-1} and 322 cm^{-1}. The most intense bands (E_g-like modes [61]) are located at about 152 cm^{-1}, 163 cm^{-1} and 213 cm^{-1}, and mainly involve in-plane vibrations of Re atoms [61].

The XANES spectra for bulk ReS_2 and GaN-ReS_2, ZnS-ReS_2 and ZnO-ReS_2 *core-shell* NWs are close (Fig. 6). They are dominated by a strong

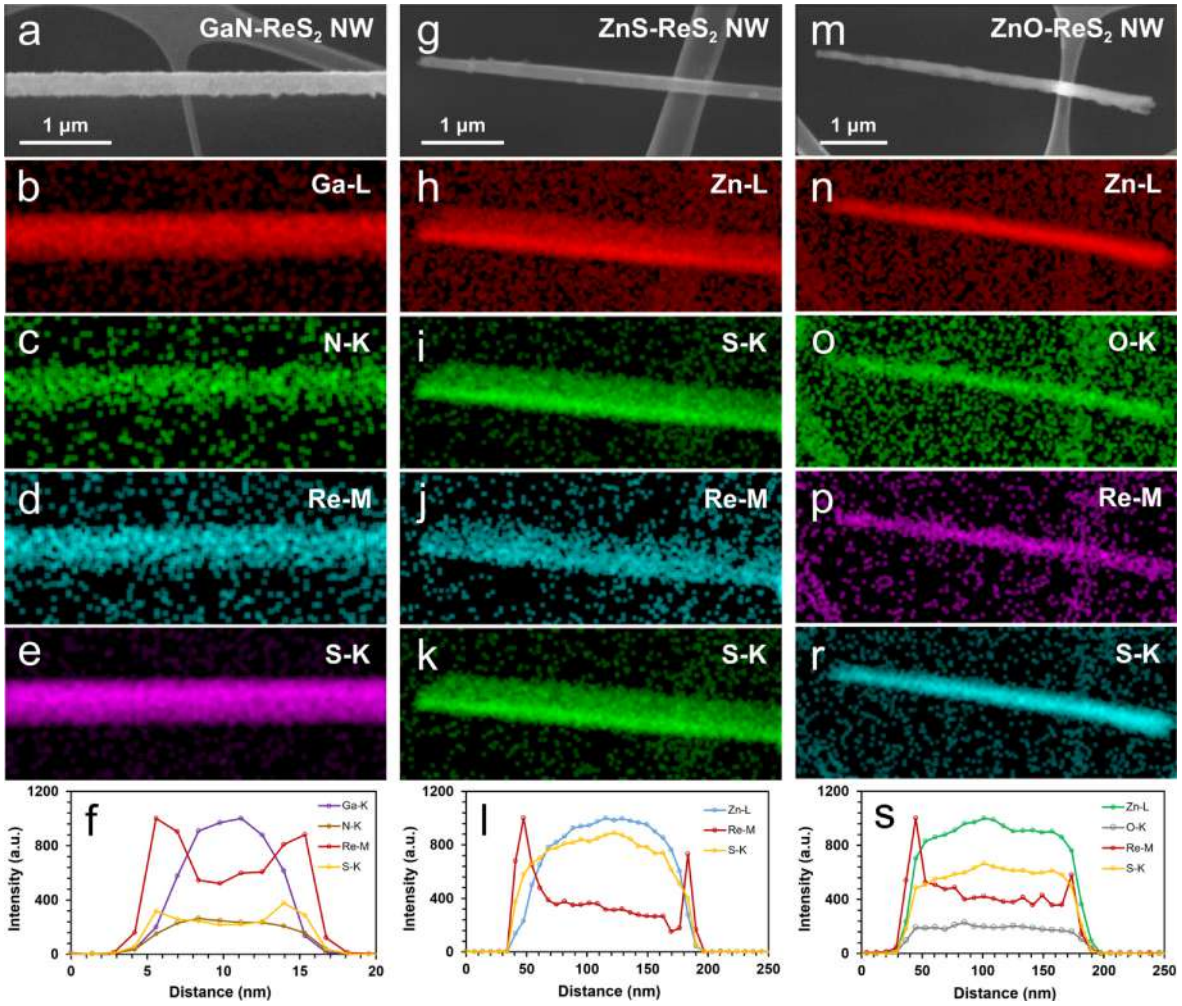

Fig. 3. EDX elemental mapping of (a-f) GaN-ReS_2, (g-l) ZnS-ReS_2 and (m-s) ZnO-ReS_2 *core-shell* nanowires. The mapping was performed in SEM, and shows the uniform distribution of the ReS_2 shell along the nanowire, while cross-sectional line scans obtained via TEM confirm the distinct interfaces of the *core-shell* structure.

"white line" at 10542 eV due to the $2p_{3/2}$(Re) → 5d(Re)-3p(S) dipole allowed transition. The low signal/noise ratio for the ZnO-ReS_2 sample is due to the small amount present. Note that the Ga K-edge XANES was also collected for GaN-ReS_2 NWs due to the close proximity of the Ga (10367 eV) and Re (10535 eV) absorption edges. This result is in agreement with that reported for GaN NWs in [62].

The Re L_3-edge XANES for bulk ReS_2 agrees well with the data in the literature [63]. We interpreted it using the results of *ab initio* XANES calculations using the finite difference method (FDM) as implemented in the FDMNES code [64]. The XANES spectra were calculated for the ReS_2 crystallographic structure taken from [65] by averaging over four non-equivalent rhenium atoms in the unit cell. Relativistic calculations were performed using a self-consistent potential for atomic cluster radii up to 5 Å. The real energy-dependent exchange Hedin-Lundqvist potential was employed, and the calculated XANES spectra were broadened by natural core-level width ($\Gamma(L_3\text{-Re}) = 5.04$ eV). The results are shown in Fig. 6(a).

The results of the *ab initio* Re L_3-edge XANES simulations of bulk ReS_2 by the FDMNES code are shown in Fig. 6(b). It can be seen that a cluster with a radius of 4.0 Å around the absorbing rhenium atom is sufficient to reproduce the experimental XANES. The white line located at about 2 eV above the Fermi level E_F and the two maxima at about 50 and 110 eV in Fig. 6(b) are due to the interaction between the excited photoelectron and six sulfur atoms at 2.3–2.5 Å, which form the first coordination shell of the absorbing rhenium atom. The shoulder located at 10 eV appears after the addition of the second coordination shell, composed of four rhenium atoms at 2.8–3.6 Å, and it becomes more pronounced with the addition of subsequent outer shells. Thus, the Re L_3-edge XANES of ReS_2 is determined mainly by the local atomic structure, which explains its similarity in both *core-shell* NWs and in the bulk (Fig. 6(a)).

Fig. 7 compares the total and projected densities of states (PDOSs) calculated for [0001]-oriented monolayered (ML) and three-layered (3ML) ReS_2 nanosheets, as shown in Fig. 7(a) and 7(b), respectively, and the PDOSs calculated for slab models of [1 –1 0 0] oriented ZnS, ZnO, and GaN NWs (Fig. 7(c), 7(d), and 7(e), respectively). The PDOS calculated for bi-layered (2ML) ReS_2 nanosheet is not presented in Fig. 7, as its electronic structure does not differ in practise from that calculated for 3ML ReS_2. For all of the ReS_2 nanosheets under study, the upper part of the valence band (VB) is predominantly formed by the S (3p) orbitals, with significant contributions from the Re (5d) orbitals. The bottom of the conduction band (CB) for the ReS_2 nanosheets is formed mainly of the Re (5d) states. In the case of the ZnS, ZnO and GaN (1 –1 0 0) surfaces, the top of the VB is formed of the O or N 2p states, while the 3d orbitals of Zn and Ga mainly form the bottom of the CB. It can clearly be seen that the band edge positions of ML and 3ML ReS_2 differ from those of the bulk (Fig. S6(a)). The bottom of the CB is shifted down, closer to the hydrogen evolution potential of −4.44 eV, while the position of the top of the VB calculated for the (1 –1 0 0) surfaces of ZnO, ZnS, and GaN NWs is located near the oxygen reduction potential of −5.67 eV. The band alignment is shown schematically in Fig. 8. This allows us to conclude that the hybrid *core-shell* ZnO-ReS_2,

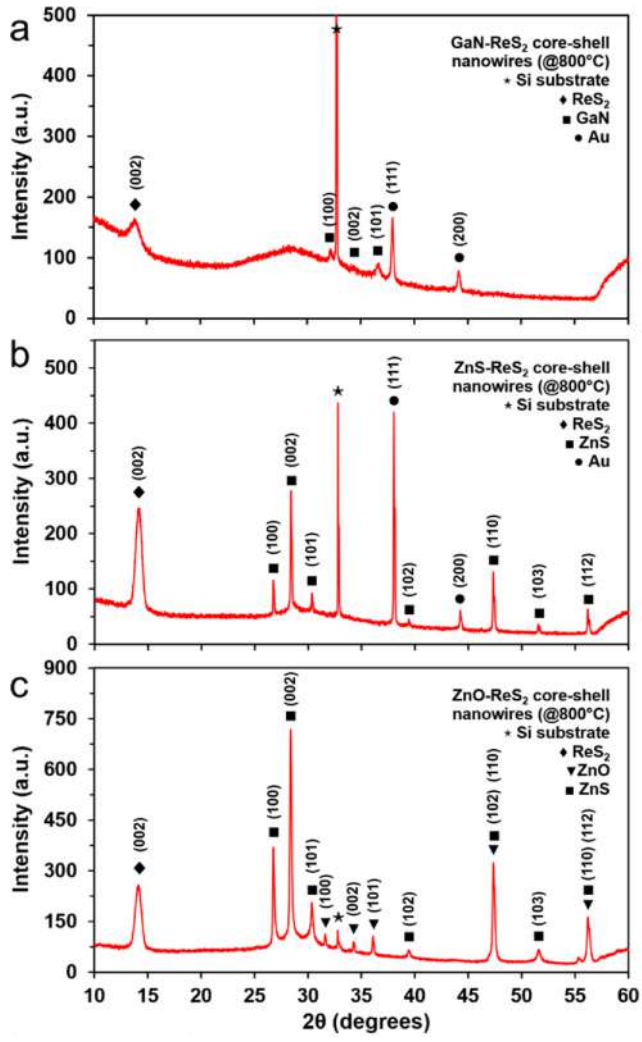

Fig. 4. X-ray diffraction patterns of as-grown (a) GaN-ReS_2, (b) ZnS-ReS_2, and (c) ZnO-ReS_2 *core-shell* nanowire arrays on Si(1 0 0)/SiO_2 substrates, prepared at 800 °C. Note the ZnS phase peaks in the ZnO-ReS_2 pattern, which emerge due to a partial or full conversion of ZnO to ZnS starting at around 750 °C.

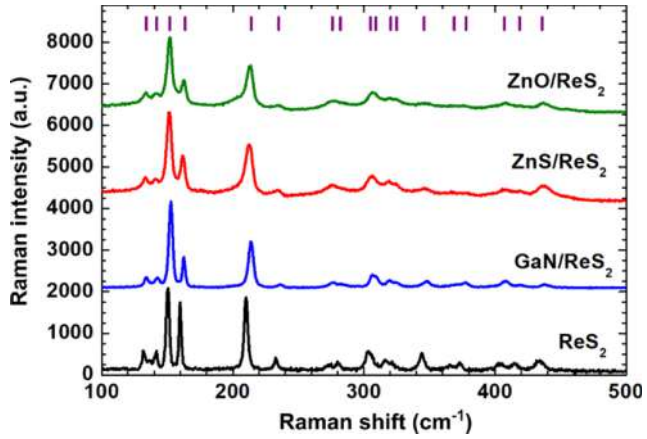

Fig. 5. Micro-Raman scattering spectra for as-grown ZnO-ReS_2, ZnS-ReS_2 and GaN-ReS_2 *core-shell* nanowires, prepared at 800 °C, and bulk ReS_2. Vertical lines indicate the positions of the Raman active A_g phonon modes.

ZnS-ReS_2, and GaN-ReS_2 NWs can be considered promising potential materials for efficient solar-driven photo(electro)catalytic water splitting.

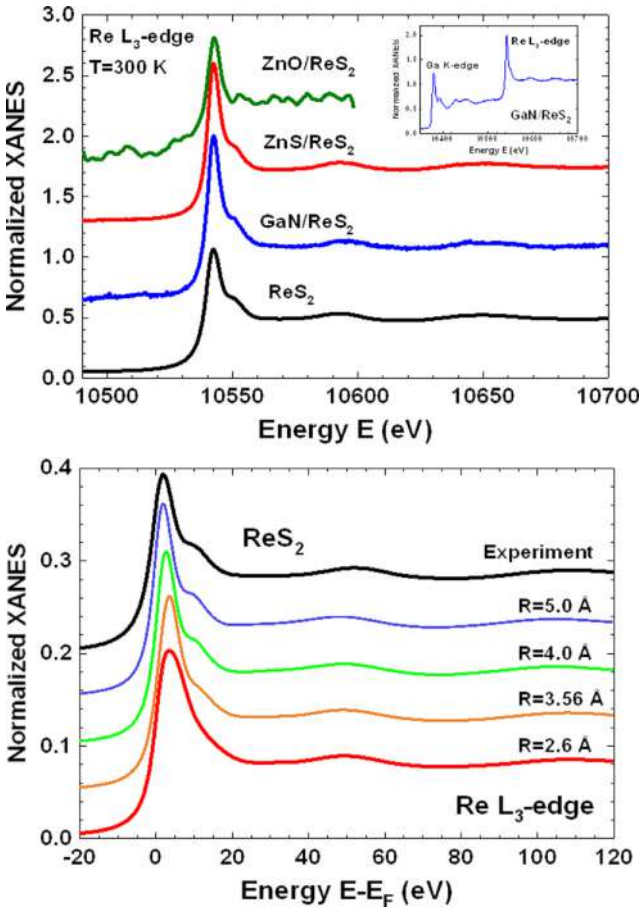

Fig. 6. (a) X-ray absorption near edge structure (XANES) spectra for bulk ReS_2 and GaN-ReS_2, ZnS-ReS_2 and ZnO-ReS_2 *core-shell* nanowires measured at the Re L_3-edge. The inset shows the full acquired XANES spectrum for GaN-ReS_2 nanowires including the Ga K-edge, which is located about 160 eV below the Re L_3-edge. (b) Results of the *ab initio* Re L_3-edge XANES simulations for bulk ReS_2, performed for atomic clusters with radius R from 2.6 to 5.0 Å. The XANES spectra in (a) and (b) are vertically shifted for clarity.

4. Conclusions

In this study, we have demonstrated the possibility of using two-step growth process for few-layer ReS_2 on different semiconductor material NWs. An amorphous rhenium oxide coating was deposited on the substrates by reactive DC magnetron sputtering, followed by sulfurization of the pre-deposited film at different temperatures. High-quality monocrystalline few-layer ReS_2 was successfully grown on GaN and ZnS NWs at a sulfurization temperature of 800 °C, although it was only possible to obtain a polycrystalline ReS_2 shell on ZnO NWs at lower temperatures, due to the conversion of ZnO to the ZnS phase at 750 °C. The obtained *core-shell* heterostructures were characterized in detail using XRD, SEM, TEM, EDX, micro-Raman spectroscopy and X-ray absorption spectroscopy, and experimental characterizations were supported by total energy calculations of the electronic structure for the studied materials. We showed that in a similar way to other TMDs such as MoS_2 and WS_2, few-layer ReS_2 can be obtained by sulfurization of a pre-deposited rhenium oxide film. Our results demonstrate the potential of using NWs as a template for the growth of layered vdW materials to produce novel hybrid *core-shell* nanostructures that have a number of potential applications, such as in electronics, optoelectronics and various energy applications.

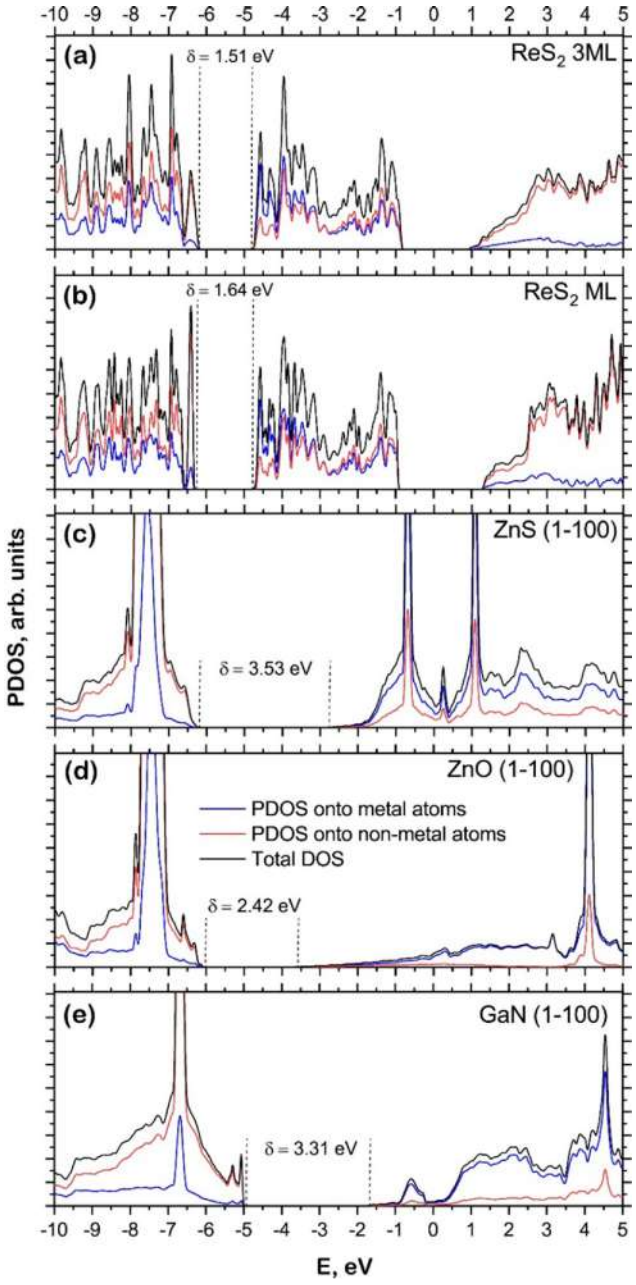

Fig. 7. Total and projected densities of states (PDOSs) calculated for (a) 3-monolayer-thick ReS_2 nanosheet, (b) monolayer-thick ReS_2 nanosheet, (c) ZnS (1 –1 0 0) slab, (d) ZnO (1 –1 0 0) slab, and (e) GaN (1 –1 0 0) slab. The 24-layer thick slabs are symmetrically terminated to mimic the surface of the nanowires. PDOSs are projected onto all orbitals of the corresponding metal or non-metal atoms. The energy scale is shown with respect to the vacuum level.

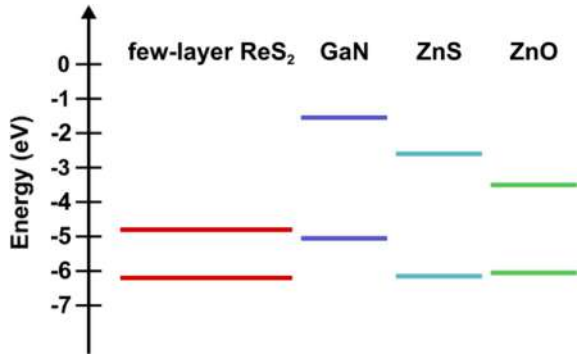

Fig. 8. Schematic representation of the heterostructure band alignment, based on the DFT calculations performed here.

CRediT authorship contribution statement

Edgars Butanovs: Methodology, Validation, Investigation, Visualization, Writing - original draft. **Alexei Kuzmin:** Investigation, Formal analysis, Visualization. **Sergei Piskunov:** Methodology, Formal analysis, Visualization. **Krisjanis Smits:** Investigation. **Aleksandr Kalinko:** Investigation. **Boris Polyakov:** Conceptualization, Supervision, Investigation, Writing - review & editing.

Declaration of Competing Interest

The authors declare that they have no known competing financial interests or personal relationships that could have appeared to influence the work reported in this paper.

Acknowledgements

This research was funded by the ERDF project “Smart Metal Oxide Nanocoatings and HIPIMS Technology”, project number: 1.1.1.1/18/A/073. Institute of Solid State Physics, University of Latvia as the Center of Excellence has received funding from the European Union’s Horizon 2020 Framework Programme H2020-WIDESPREAD-01-2016-2017-TeamingPhase2 under grant agreement No. 739508, project CAMART2.

Appendix A. Supplementary material

Supplementary information is available containing XRD and SEM data for the pure NWs used in the experiments and the ReS_2 thin films, SAED patterns and analysis of the as-grown *core-shell* NWs, TEM images of GaN-ReS_2 and ZnO-ReS_2 NWs at different annealing temperatures, and PDOSs calculated for the bulk phases of ReS_2, ZnS, ZnO, and GaN crystals. Supplementary data to this article can be found online at https://doi.org/10.1016/j.apsusc.2020.147841.

References

[1] K.S. Novoselov, et al., A roadmap for graphene, Nature 490 (2012) 192–200.
[2] Q.H. Wang, K. Kalantar-Zadeh, A. Kis, J.N. Coleman, M.S. Strano, Electronics and optoelectronics of two-dimensional transition metal dichalcogenides, Nat. Nanotechnol. 7 (2012) 699–712.
[3] M. Chhowalla, et al., The chemistry of two-dimensional layered transition metal dichalcogenide nanosheets, Nat. Chem. 5 (2012) 263–275.
[4] D.L. Duong, S.J. Yun, Y.H. Lee, Van der Waals layered materials: Opportunities and challenges, ACS Nano 11 (2017) 11803–11830.
[5] W. Choi, et al., Recent development of two-dimensional transition metal dichalcogenides and their applications, Mater. Today 20 (2017) 116–130.
[6] F. Wang, et al., Progress on electronic and optoelectronic devices of 2D Layered semiconducting materials, Small 13 (2017) 1604298.
[7] P.K. Kannan, D.J. Late, H. Morgan, C.S. Rout, Recent developments in 2D layered inorganic nanomaterials for sensing, Nanoscale 7 (2015) 13293–13312.
[8] J. Di, et al., Ultrathin two-dimensional materials for photo- and electrocatalytic hydrogen evolution, Mater. Today 21 (2018) 749–770.
[9] M.I. Bakti Utama, et al., Recent developments and future directions in the growth of nanostructures by van der Waals epitaxy, Nanoscale 5 (2013) 3570.
[10] K.S. Novoselov, A. Mishchenko, A. Carvalho, A.H. Castro Neto, 2D materials and van der Waals heterostructures, Science 353 (2016) aac9439.
[11] T. Zhang, et al., Twinned growth behaviour of two-dimensional materials, Nat. Commun. 7 (2016) 13911.
[12] K. Kang, et al., Layer-by-layer assembly of two-dimensional materials into wafer-scale heterostructures, Nature 550 (2017) 229–233.
[13] M. Rahman, K. Davey, S.-Z. Qiao, Advent of 2D rhenium disulfide (ReS2): Fundamentals to applications, Adv. Funct. Mater. 27 (2017) 1606129.
[14] Z. Chen, et al., Core–shell MoO3 –MoS2 Nanowires for hydrogen evolution: A functional design for electrocatalytic materials, Nano Lett. 11 (2011) 4168–4175.
[15] N. Choudhary, et al., High-performance one-body core/shell nanowire supercapacitor enabled by conformal growth of capacitive 2D WS2 layers, ACS Nano 10 (2016) 10726–10735.
[16] Q. Yun, et al., Layered transition metal dichalcogenide-based nanomaterials for electrochemical energy storage, Adv. Mater. 32 (2020) 1903826.

[17] X. Wang, et al., Boosting the stable sodium-ion storage performance by tailoring the 1D TiO2@ReS2 core-shell heterostructures, Electrochim. Acta 338 (2020) 135695.
[18] Y. Li, F. Qian, J. Xiang, C.M. Lieber, Nanowire electronic and optoelectronic devices, Mater. Today 9 (2006) 18–27.
[19] R. Yan, D. Gargas, P. Yang, Nanowire photonics, Nat. Photonics 3 (2009) 569–576.
[20] L.J. Lauhon, M.S. Gudiksen, D. Wang, C.M. Lieber, Epitaxial core–shell and core–multishell nanowire heterostructures, Nature 420 (2002) 57–61.
[21] Y. Dong, B. Tian, T.J. Kempa, C.M. Lieber, Coaxial group III−nitride nanowire photovoltaics, Nano Lett. 9 (2009) 2183–2187.
[22] E. Butanovs, A. Kuzmin, J. Butikova, S. Vlassov, B. Polyakov, Synthesis and characterization of ZnO/ZnS/MoS2 core-shell nanowires, J. Cryst. Growth 459 (2017) 100–104.
[23] F. Chen, T. Wang, L. Wang, X. Ji, Q. Zhang, Improved light emission of MoS2 monolayers by constructing AlN/MoS2 core–shell nanowires, J. Mater. Chem. C 5 (2017) 10225–10230.
[24] B. Polyakov, et al., Unexpected epitaxial growth of a few WS2 layers on $1\bar{1}00$ facets of ZnO nanowires, J. Phys. Chem. C 120 (2016) 21451–21459.
[25] E. Butanovs, Fast-response single-nanowire photodetector based on ZnO/WS2 core/shell heterostructures, ACS Appl. Mater. Interfaces 10 (2018) 13869–13876.
[26] E. Zhang, et al., ReS2-Based field-effect transistors and photodetectors, Adv. Funct. Mater. 25 (2015) 4076–4082.
[27] C. Gong, et al., Electronic and optoelectronic applications based on 2D novel anisotropic transition metal dichalcogenides, Adv. Sci. 4 (2017) 1700231.
[28] Y.-C. Lin, et al., Single-layer ReS2: Two-dimensional semiconductor with tunable in-plane anisotropy, ACS Nano 9 (2015) 11249–11257.
[29] O.B. Aslan, D.A. Chenet, A.M. van der Zande, J.C. Hone, T.F. Heinz, Linearly polarized excitons in single- and few-layer ReS2 crystals, ACS Photonics 3 (2016) 96–101.
[30] B.C. Lee, et al., Probing distinctive electron conduction in multilayer rhenium disulfide, Adv. Mater. 31 (2018) 1805860.
[31] H. Jang, C.R. Ryder, J.D. Wood, M.C. Hersam, D.G. Cahill, 3D anisotropic thermal conductivity of exfoliated rhenium disulfide, Adv. Mater. 29 (2017) 1700650.
[32] C. An, et al., The opposite anisotropic piezoresistive effect of ReS2, ACS Nano 13 (2019) 3310–3319.
[33] F. Liu, et al., Highly sensitive detection of polarized light using anisotropic 2D ReS2, Adv. Funct. Mater. 26 (2016) 1169–1177.
[34] C.M. Corbet, et al., Field effect transistors with current saturation and voltage gain in ultrathin ReS2, ACS Nano 9 (2015) 363–370.
[35] S. Yang, J. Kang, Q. Yue, J.M.D. Coey, C. Jiang, Defect-modulated transistors and gas-enhanced photodetectors on ReS2 nanosheets, Adv. Mater. Interfaces 3 (2016) 1500707.
[36] X. Li, et al., Controlled growth of large-area anisotropic ReS2 atomic layer and its photodetector application, Nanoscale 8 (2016) 18956–18962.
[37] J. Shim, et al., High-performance 2D rhenium disulfide (ReS2) transistors and photodetectors by oxygen plasma treatment, Adv. Mater. 28 (2016) 6985–6992.
[38] B. Kang, Y. Kim, W.J. Yoo, C. Lee, Ultrahigh photoresponsive device based on ReS2/graphene heterostructure, Small 14 (2018) 1802593.
[39] E. Liu, et al., Integrated digital inverters based on two-dimensional anisotropic ReS2 field-effect transistors, Nat. Commun. 6 (2015) 6991.
[40] P.K. Srivastava, et al., Van der Waals broken-gap p–n heterojunction tunnel diode based on black phosphorus and rhenium disulfide, ACS Appl. Mater. Interfaces 11 (2019) 8266–8275.
[41] W. Huang, et al., Ion beam defect engineering on ReS2/Si photocathode with significantly enhanced hydrogen evolution reaction, Adv. Mater. Interfaces 6 (2019) 1801663.
[42] X. He, et al., Chemical vapor deposition of high-quality and atomically layered ReS2, Small 11 (2015) 5423–5429.
[43] S. Zhang, et al., Facile synthesis of rhenium disulfide flakes by vacuum vapor transport method, Mater. Res. Bull. 111 (2019) 191–194.
[44] J. Seo, J. Lee, G. Jeong, H. Park, Site-selective and van der Waals epitaxial growth of rhenium disulfide on graphene, Small 15 (2019) 1–7.
[45] J.-K. Qin, et al., Van der Waals epitaxy of large-area continuous ReS2 films on mica substrate, RSC Adv. 7 (2017) 24188–24194.
[46] F. Cui, et al., Tellurium-assisted epitaxial growth of large-area, highly crystalline ReS2 atomic layers on mica substrate, Adv. Mater. 28 (2016) 5018.
[47] Y.-C. Lin, et al., Wafer-scale MoS2 thin layers prepared by MoO3 sulfurization, Nanoscale 4 (2012) 6637.
[48] C.-R. Wu, et al., Establishment of 2D Crystal heterostructures by sulfurization of sequential transition metal depositions: Preparation, characterization, and selective growth, Nano Lett. 16 (2016) 7093–7097.
[49] H. Bark, et al., Large-area niobium disulfide thin films as transparent electrodes for devices based on two-dimensional materials, Nanoscale 10 (2018) 1056–1062.
[50] H.R. Gutiérrez, et al., Extraordinary room-temperature photoluminescence in triangular WS2 monolayers, Nano Lett. 13 (2013) 3447–3454.
[51] N. Urakami, T. Okuda, Y. Hashimoto, Epitaxial growth of ReS2 (001) thin film via deposited-Re sulfurization, Jpn. J. Appl. Phys. 57 (2018) 02CB07.
[52] G. Suo, S. Jiang, J. Zhang, J. Li, M. He, Synthetic strategies and applications of GaN nanowires, Adv. Condens. Matter Phys. 2014 (2014) 1–11.
[53] X. Fang, et al., ZnS nanostructures: From synthesis to applications, Prog. Mater. Sci. 56 (2011) 175–287.
[54] M. Klinger, More features, more tools, more CrysTBox, J. Appl. Crystallogr. 50 (2017) 1226–1234.
[55] W.A. Caliebe, V. Murzin, A. Kalinko, M. Görlitz, High-flux XAFS-beamline P64 at PETRA III, AIP Conf. Proc. (2019, 2054,) 060031.
[56] J. Heyd, G.E. Scuseria, M. Ernzerhof, Hybrid functionals based on a screened Coulomb potential, J. Chem. Phys. 118 (2003) 8207–8215.
[57] R. Dovesi, et al., Quantum-mechanical condensed matter simulations with CRYSTAL, Wiley Interdiscip. Rev. Comput. Mol. Sci. 8 (2018) e1360.
[58] H.J. Monkhorst, J.D. Pack, Special points for Brillouin-zone integrations, Phys. Rev. B 13 (1976) 5188–5192.
[59] C. Ho, Y. Huang, P. Liao, K. Tiong, Crystal structure and band-edge transitions of ReS2−xSex layered compounds, J. Phys. Chem. Solids 60 (1999) 1797–1804.
[60] S.K. Panda, A. Dev, S. Chaudhuri, Fabrication and luminescent properties of c-axis oriented ZnO−ZnS core−shell and ZnS nanorod arrays by sulfidation of aligned ZnO nanorod arrays, J. Phys. Chem. C 111 (2007) 5039–5043.
[61] Y. Feng, et al., Raman vibrational spectra of bulk to monolayer ReS2 with lower symmetry, Phys. Rev. B 92 (2015) 054110.
[62] J.W. Chiou, et al., Electronic structure of GaN nanowire studied by x-ray-absorption spectroscopy and scanning photoelectron microscopy, Appl. Phys. Lett. 82 (2003) 3949–3951.
[63] Y. Takahashi, An atomic level study of rhenium and radiogenic osmium in molybdenite, Geochim. Cosmochim. Acta 71 (2007) 5180–5190.
[64] O. Bunău, Y. Joly, Self-consistent aspects of x-ray absorption calculations, J. Phys. Condens. Matter 21 (2009) 345501.
[65] H.-J. Lamfers, A. Meetsma, G.A. Wiegers, J.L. de Boer, The crystal structure of some rhenium and technetium dichalcogenides, J. Alloys Compd. 241 (1996) 34–39.